# High-Performance, Highly Bendable MoS₂ Transistors with High-K Dielectrics for Flexible Low-Power Systems

Hsiao-Yu Chang,[†] Shixuan Yang,[‡] Jongho Lee,[†] Li Tao,[†] Wan-Sik Hwang,[§] Debdeep Jena,[§] Nanshu Lu,[‡] and Deji Akinwande[†,*]

[†]Microelectronics Research Center and the Department of Electrical and Computer Engineering, The University of Texas at Austin, Austin, Texas 78758, United States, [‡]Department of Aerospace Engineering and Engineering Mechanics, The University of Texas at Austin, Austin, Texas 78712, United States, and [§]Department of Electrical Engineering, University of Notre Dame, Notre Dame, Indiana 46556, United States

ABSTRACT While there has been increasing studies of MoS₂ and other two-dimensional (2D) semiconducting dichalcogenides on hard conventional substrates, experimental or analytical studies on flexible substrates has been very limited so far, even though these 2D crystals are understood to have greater prospects for flexible smart systems. In this article, we report detailed studies of MoS₂ transistors on industrial plastic sheets. Transistor characteristics afford more than 100x improvement in the ON/OFF current ratio and 4x enhancement in mobility compared to previous flexible MoS₂ devices. Mechanical studies reveal robust electronic properties down to a bending radius of 1 mm which is comparable to previous reports for flexible graphene transistors. Experimental investigation identifies that crack formation in the dielectric is the responsible failure mechanism demonstrating that the mechanical properties of the dielectric layer is critical for realizing flexible electronics that can accommodate high strain. Our uniaxial tensile tests have revealed that atomic-layer-deposited HfO₂ and Al₂O₃ films have very similar crack onset strain. However, crack propagation is slower in HfO₂ dielectric compared to Al₂O₃ dielectric, suggesting a subcritical fracture mechanism in the thin oxide films. Rigorous mechanics modeling provides guidance for achieving flexible MoS₂ transistors that are reliable at sub-mm bending radius.
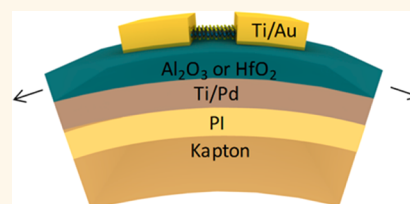
KEYWORDS: MoS₂ · flexible transistor · polyimide · graphene · field-effect transistor · transition metal dichalcogenides · mobility · bending radius · crack formation · critical strain

Future ubiquitous smart electronic systems are envisioned to afford arbitrary form factors, robust elasticity, high speed charge transport, and low-power consumption, a combined set of attributes that transcend existing Si-based electronics.[1−3] Ideally, these smart systems will be integrated and realized seamlessly on environmentally friendly flexible or plastic substrates. A major contemporary challenge concerns the choice of the semiconducting material suitable for high-performance field-effect transistors (FETs) on a flexible substrate.[1,2,4] In the past decade, organic and amorphous silicon have been widely explored but their carrier mobilities (typically ≤1 cm²/V·s) are too low for high-speed transistors operating at nanosecond cycles.[1,4] More recently, graphene has attracted substantial interest for high-performance flexible electronics owing to its high carrier mobility (>10 000 cm²/V·s) and

outstanding radio frequency properties;[5−10] however, its lack of a bandgap is a major drawback since low-power switching or digital transistors cannot be realized.[11] This drawback has consequently motivated the search for other layered atomic sheets with substantial bandgaps such as the semiconducting transition metal dichalcogenides (TMDs).[12,13]

Molybdenum disulfide (MoS₂) is a prototypical TMD that has been attracting rapidly growing interest owing to its large semiconducting bandgap (∼1.8 eV for monolayer and ∼1.3 eV for bulk films), which is ideal for low-power electronics on hard and soft substrates.[12,14−18] In addition, its reported high carrier mobility (up to 200 cm²/V·s at room temperature),[17] high strength,[19] and large surface to volume ratio make it a compelling semiconducting nanomaterial for high speed flexible transistors and sensors. Pu *et al.* reported a flexible MoS₂ FET with ion-gel
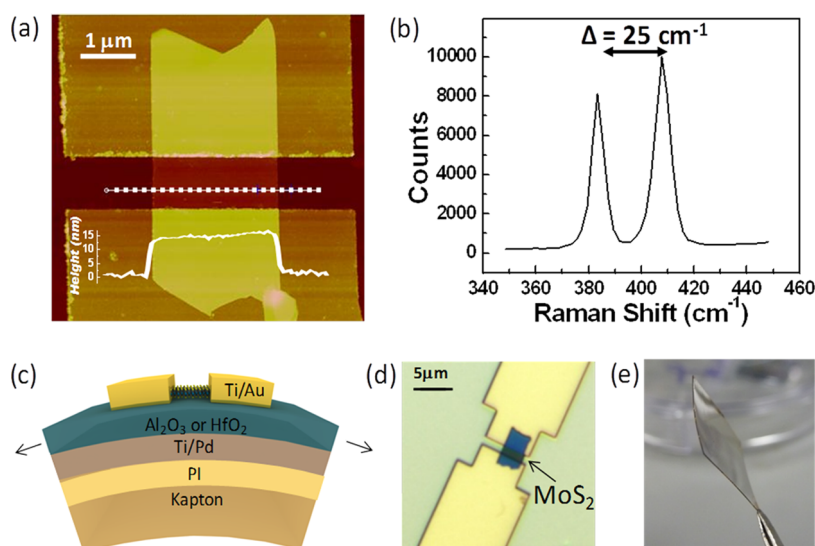
Figure 1. (a) AFM analysis shows the thickness of a MoS_2 flake which is around 15 nm. The height profile of MoS_2 flake is scanned along the dotted line. (b) From the Raman spectrum of the MoS_2 flake, the peak spacing between the E^1_{2g} and A^1_g vibration mode is 25 cm^{-1} confirming that the MoS_2 flake is a multilayer film.[28] (c) The schematic depiction of the flexible bottom gate device structure. (d) The optical microscope picture for the MoS_2 device after the S/D patterned by e-beam lithography. The channel length is 1 μm and the MoS_2 flake with thickness of around 10 nm shows dark blue color in the optical image. (e) The photograph of the flexible sample made on industrial polyimide sheet with cured liquid PI on the surface (total thickness is $\sim$102 μm).

gate dielectric that showed high flexibility.[16] However, the low cutoff frequency ($\sim$<1 kHz)[16,20,21] of ion-gel dielectric materials essentially precludes their use in high-speed flexible transistors and hence, cannot take advantage of the carrier speed benefits of MoS_2. Yoon *et al.* adopted wet transfer approach involving the transfer of prefabricated graphene-contacted MoS_2 on SiO_2/Si onto a prefabricated polyethylene terephthalate (PET) substrate with a thick polymer gate dielectric and ITO as gate metal.[18] While it is an attractive approach for transparent electronics, the high resistance of graphene and ITO compared to normal metals limit the prospect of this device structure for high-speed flexible electronics due to excessive energy dissipation in the lossy electrodes.

In this work, we report the first comprehensive studies of MoS_2 FETs using conventional solid-state high-k dielectrics on flexible substrates, and provide guidance for scaling the bendability of this system. Our studies yield the highest ON/OFF switching ratio (>10^7), highest mobilities ($\sim$30 cm^2/V-s), highest gate control (subthreshold slope $\sim$82 mV/decade), and intrinsic gain above 100 on flexible substrates at ambient conditions. Furthermore, a study of the device mechanical flexibility reveals robust characteristics down to a bending radius of 1 mm. Comparative studies of the two high-k dielectrics (Al_2O_3 and HfO_2) used in this research determine that crack formation in the dielectric is the failure mechanism. The crack propagation velocity is substantially reduced in HfO_2 owing to its lower Young's modulus,[22−24] which in addition to its higher permittivity, suggests it is a superior gate dielectric in terms of both electrical and mechanical properties particularly under momentary

tensile strain. These results indicate that MoS_2 is likely the most suitable semiconducting material for flexible electronics and smart systems that require both low-power and high speed device characteristics.

RESULTS AND DISCUSSION

Because of the present challenge of synthesizing high-quality continuous layers of MoS_2 uniformly across a substrate,[25−27] MoS_2 devices were prepared by mechanical exfoliation from commercial crystals (SPI supplies) onto the flexible substrate for this study. Flakes with thickness between 7.9 and 23.5 nm were selected by optical microscope and confirmed by atomic force microscope (AFM). Figure 1a shows the AFM analysis for a MoS_2 flake with thickness of around 15 nm. The Raman spectroscopy (Figure 1b) shows the peak spacing between the E^1_{2g} and A^1_g vibration mode is 25 cm^{-1}, which indicates that the flake has four or more layers.[28] Figure 1c,d shows the schematic depiction and the optical microscope image of the MoS_2 device made on polyimide. Figure 1e displays the photograph of the fabricated flexible sample.

Electrical characteristics of the flexible MoS_2 FETs were then evaluated under ambient conditions. Representative transfer (I_D−V_G) characteristics are shown in Figure 2a,b. The extracted low-field mobility of the fastest device is 30 cm^2/(V·s) (Figure 2c) using the Y-function method which is defined as $I_D/\sqrt{g_m}$ (I_D is the drain current, g_m is the transconductance) and is especially suitable for studying device physics because it excludes the contact resistance effect on the mobility.[29,30] The details of the mobility extraction are provided in the Supporting Information (Figure S2 and S3 in the Supporting Information). Our
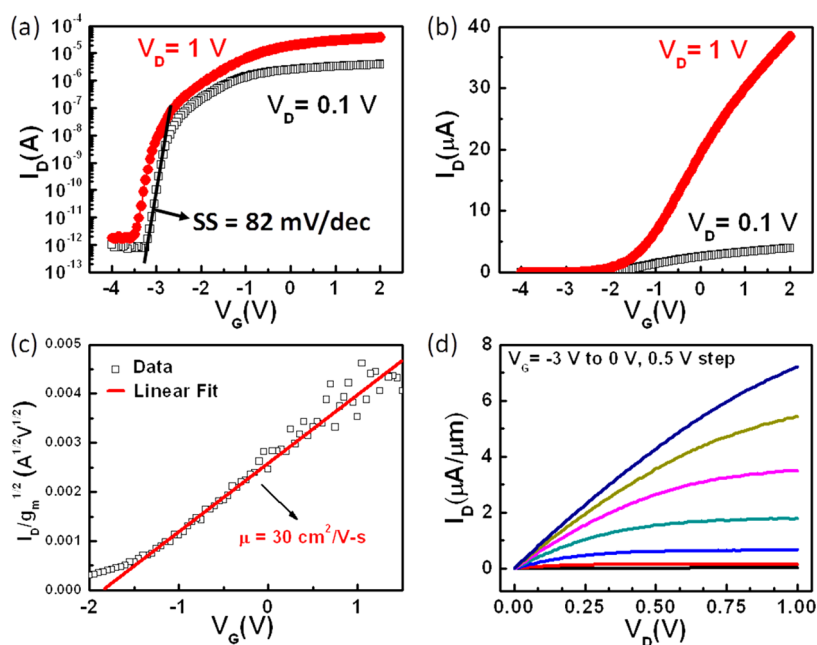
Figure 2. A representative MoS_2 FET (W/L = 3/1 μm) made with Al_2O_3 as gate dielectric on flexible PI. (a) I_D-V_G characteristics in log scale. The ON/OFF current ratio is more than 7 orders of magnitude, and the subthreshold slope (SS) is $\sim$82 mV/decade. (b) I_D-V_G characteristics in linear scale. (c) The experimental Y-function (=$I_D/\sqrt{g_m}$) profile showing the characteristic linear profile for extracting the low-field mobility. The extracted low-field mobility is 30 cm^2/(V·s). (d) I_D-V_D characteristics indicates negligible Schottky barrier in the linear region, and current saturation at high fields.

studies of the mobility—thickness dependence reveals an inverse relation (see Figure S4 in the Supporting Information), in agreement with a prior study over a similar thickness range.[17] The ON/OFF switching ratio is more than 10[7], and the subthreshold slope is $\sim$82 mV/decade. Output (I_D-V_D) characteristics shows negligible Schottky barrier in the linear region, and current saturation at high fields as shown in Figure 2d. In addition, the device intrinsic gain (g_m/g_{ds}) exceeded 100, an important metric for small-signal amplification (see Figure S5 in the Supporting Information). These device characteristics represent the state-of-the-art for MoS_2 FETs on flexible substrates, with 4× higher mobility and >100× greater ON/OFF ratio compared to a previously reported MoS_2 device.[18] These results are comparable with unpassivated MoS_2 FETs realized on Si substrates,[14,31] indicating that its unique electrical properties can be accessed on hard and soft substrates alike which is a welcome benefit for flexible electronics. Further improvement of the device performance can be achieved by mobility enhancement through passivation with a high-k dielectric to enhance the local screening effect and suppress Coulomb scattering as previously reported,[14,31−33] and reducing the contact resistance by using low work function metals, such as Scandium, to minimize the Schottky barrier at the contact.[17] However, for flexible MoS_2, the device passivation entails further research beyond what has been achieved on hard substrates, requiring not just the investigation of dielectric films with high-permittivity but also consideration of its mechanical properties in

order to ensure no detrimental impact to device flexibility and elasticity as we will elucidate subsequently. This will involve investigation of the parameter space of the passivation material including thickness, stiffness, permittivity and adhesion to the TMD to prevent delamination or early cracking under deformation.

Tensile strain is applied to the devices by convexly bending the flexible substrate using a home-built mechanical bending fixture (Figure 3a). Electrical measurements were then undertaken in order to examine the stability of several device parameters that had been subjected to the strain condition. The device parameters include mobility, ON current, and ON/OFF switching ratio. A study of the mechanical flexibility of ten devices was conducted in order to arrive at conclusions. Owing to the random orientation of MoS_2 prepared by mechanical exfoliation, the direction of the tensile strain cannot be precisely controlled. Orientation measurements of the devices indicate that they are aligned or typically within 35° of the channel length direction (the current conducting direction). The devices were held for 10 s at each bending radius, and then released for the measurement. The precise direction of the applied strain is not critical in this study, because the devices fail due to mechanical fatigue of the dielectric as evidenced by crack formation which we will discuss shortly afterward. For our work and purpose, all our devices were mechanically bent until device failure was observed which allowed us to complete our mechanical modeling studies. Future studies will aim to evaluate the electrical performance
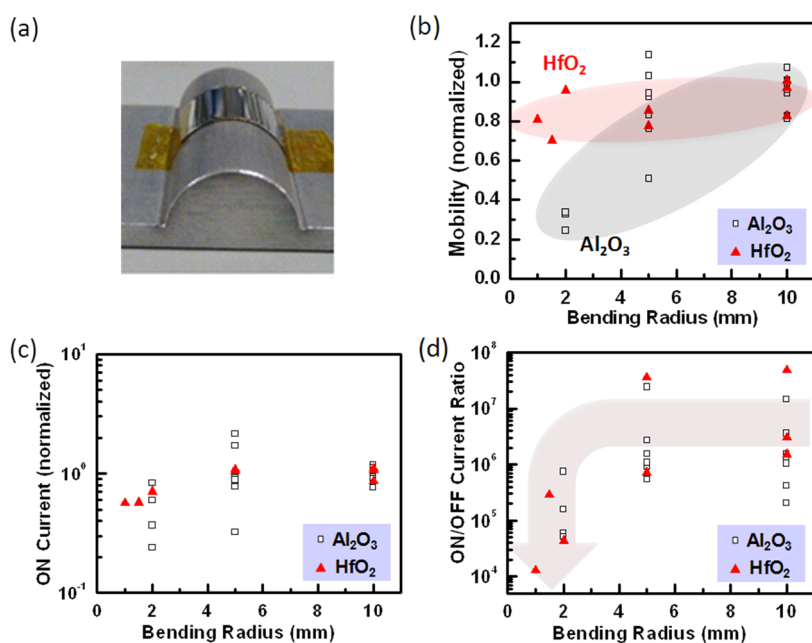
Figure 3. A study of the mechanical flexibility of MoS$_2$ FETs with Al$_2$O$_3$ and HfO$_2$ gate dielectrics. (a) The photograph of the flexible MoS$_2$ sample at a bending radius of 5 mm on the experimental bending fixture. (b and c) The dependence of the normalized low-field mobility (V_D = 0.1 V) and ON current (V_D = 1 V) on the bending radius, respectively. Mechanically robust devices provide functional electrical characteristics down to a bending radius of 1 mm for HfO$_2$ dielectric and 2 mm for Al$_2$O$_3$ dielectric. (d) The ON/OFF current ratio (V_D = 1 V) *versus* bending radius is greater than 10^4 down to 1 mm bending radius for HfO$_2$ dielectric. Substantial degradation occurs below 1 mm bending radius owing to the onset of gate dielectric failure.

and reliability of the device as a function of the number of mechanical bending cycles.

Figure 3b−d shows the dependence of the normalized mobility, normalized ON current, and ON/OFF current ratio on the bending radius respectively. Device characteristics are robust down to a bending radius of 1 mm for HfO$_2$ dielectric and 2 mm for Al$_2$O$_3$, which we attribute to the high deformability of MoS$_2$,[19] and the relatively low strain placed on the dielectric thin films. For instance, MoS$_2$ devices on HfO$_2$ retain functional properties with less than 30% mobility degradation and 10^4 ON/OFF ratio after deformation of 1 mm bending radius. At or below 2 mm bending radius, MoS$_2$ devices with Al$_2$O$_3$ dielectric show significant degradation owing to structural damage to the dielectric. Similar significant failure was observed for devices with HfO$_2$ dielectric below 1 mm bending radius, while between 2 mm and 1 mm bending radius, a gradual or soft degradation is observed. The Raman spectrum of the MoS$_2$ remains unchanged and the AFM analysis shows that MoS$_2$ with various thickness in the range of 7.9−20.1 nm remains intact after the bending test, confirming that device failure is caused by dielectric failure, but not by damage to MoS$_2$ (see Figures S6−S9 in the Supporting Information).

To unambiguously identify the mechanism responsible for device failure after severe bending, the gate dielectric structural integrity was investigated under varying tensile strains. For this purpose, HfO$_2$ and Al$_2$O$_3$ films are deposited on 26-μm-thick rectangular PI (PI-2574) strips, with a sample cross-section similar to the

device sample as illustrated in Figure 4a. Without the Kapton substrate, the thinner 26 um PI affords a greater range of tensile strain to be studied, and maintained the same surface property as the device structure. We did not perform our own measurements of the Young's modulus of each dielectric material but materials fabricated in similar conditions are measured to have E_{HfO_2} = 73.4 GPa, and $E_{Al_2O_3}$ = 163.3 GPa, respectively.[22] Stretch tests were subsequently done using a home-built mechanical test fixture in situ under optical microscope (Figure 4b). The stretch tests revealed formation of channel cracks aligned perpendicular to the stretch direction in the dielectric materials as shown in Figure 4c. Fracture in dielectrics results in increased scattering sites which degrades electron mobility and drive current. Moreover, the growing density of dielectric cracks lead to increased gate leakage and subsequent device failure. A quantitative count of the crack density as a function of the applied tensile strain can be seen in Figure 4d. The critical strain and saturation crack density are extracted using an empirical model that is applicable to this work.[34] The result suggests a slightly higher critical strain for HfO$_2$ (1.72%) compared to Al$_2$O$_3$ (1.69%). We found the crack density of HfO$_2$ saturates at slightly higher values (~10%) compared to that of Al$_2$O$_3$, which is consistent with the expectations that films with lower strength ($\sigma_{max} = E\varepsilon_{cr}$, where $\varepsilon_{cr}^{Al_2O_3} \approx \varepsilon_{cr}^{HfO_2}$ but $E_{Al_2O_3} > E_{HfO_2}$) exhibit lower saturation crack spacing.[35] We note that device failure is not determined by saturation crack density but by the onset of crack formation and
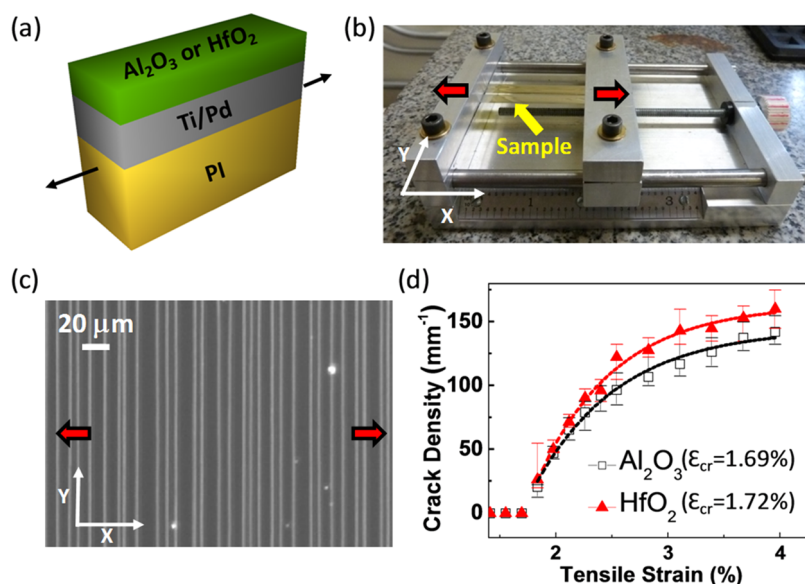
Figure 4. (a) Test structure for the stretching experiments to elucidate the mechanical reliability of selected gate dielectrics on flexible PI. (PI 26 μm/Ti 2 nm/Pd 50 nm/Al$_2$O$_3$ or HfO$_2$ 25 nm) (b) Photograph of the stretcher test fixture. The stretching direction was along the x-direction. (c) Optical microscope image of the sample of HfO$_2$ at strain ~2.5%. The parallel cracks aligned to the y-direction are due to tensile stress. (d) The dependence of the crack density on tensile strain for Al$_2$O$_3$ and HfO$_2$. The stretch test shows that the critical crack onset strain is around 1.69% and 1.72%, and the crack density saturates at 145 and 164 mm^{-1} for Al$_2$O$_3$ and HfO$_2$, respectively.

the velocity of crack propagation which we elucidate subsequently.

Time-dependent observation of the crack formation and propagation reveal that the crack propagation is substantially slower in HfO$_2$ compared to Al$_2$O$_3$ (two video recordings are provided as supplementary media files). The measured average crack propagation velocity is 4.9 and 28.4 μm/s for HfO$_2$ and Al$_2$O$_3$, respectively, which is quantitatively consistent with the exponential relation between crack growth velocity V and the energy release rate ($G \sim E\varepsilon^2$, where $\varepsilon_{cr}^{Al_2O_3} \approx \varepsilon_{cr}^{HfO_2}$ but $E_{Al_2O_3} > E_{HfO_3}$) for subcritical fracture in thin oxide films.[23,24] This measurement suggests that HfO$_2$ dielectric will be more reliable under momentary deformation while the reliability under steady-state conditions is expected to be similar.

To reveal the controlling parameters on device bendability, we perform detailed mechanics analysis in dielectric thin films accounting for both residual strain due to thermal process during sample fabrication and mechanical strain induced by the bending test. Sample fabrication involved several steps of thermal process. For example, the liquid polyimide (PI-2574) is cured at 300 °C on the Kapton substrate and the dielectric was deposited at 200 °C by ALD. Mismatch of the coefficients of thermal expansion (CTE) in the multilayers will induce residual stresses and an intrinsic curvature to the elastic multilayer stack before the bending test. The strain in the dielectric layer corresponding to the residual stress due to thermal process is named *thermal strain*, or ε_t. It can be calculated by just considering the temperature change

from the initial status to the final status of each layer,[36] as illustrated in Figure S11. The detailed calculations can be found in the Supporting Information. Figure S12 is used to derive the *bending strain*, or ε_b. Suppose the as-fabricated multilayer sample has an intrinsic radius of curvature R_1 at the neutral axis and it is then mechanically bent to R_2, if y is the distance from the dielectric layer to the neutral axis, the strain in the oxide layer due to mechanical bending is derived in the Supporting Information. Total strain (ε_{tot}) in the dielectrics is then the superposition of the thermal strain and the bending strain, *i.e.*, $\varepsilon_{tot} = \varepsilon_t + \varepsilon_b$, which corresponds to the total stress in the dielectrics. Thermal strain, bending strain, and total strain are shown graphically as functions of substrate thickness (t_s) and substrate modulus (E_s) at a given bending radius in Figure S13. It is visually revealed in the plot that although the ε_{tot} curve mainly follows the shape of the ε_b curve, the contribution from ε_t is nontrivial, and therefore cannot be omitted.

To determine the bendability of the device, *i.e.*, the minimum bending radius measured from the bottom of the device before the dielectric layer starts to crack (r_{min}), we take the criterion of $\varepsilon_{tot} = \varepsilon_{cr}$ for the dielectric layer, where ε_{cr} is the critical crack onset strain as is measured in Figure 4d. Solving this equation yields the r_{min} as a function of the thickness and Young's modulus of the substrate (t_s and E_s), as well as the thickness and Young's modulus of the dielectric layer (t_d and E_d). The result shows very weak dependence of r_{min} on t_d or E_d, but rather quite sensitive to t_s and E_s. Figure 5a shows the minimum bending radius, r_{min}, as a function of the
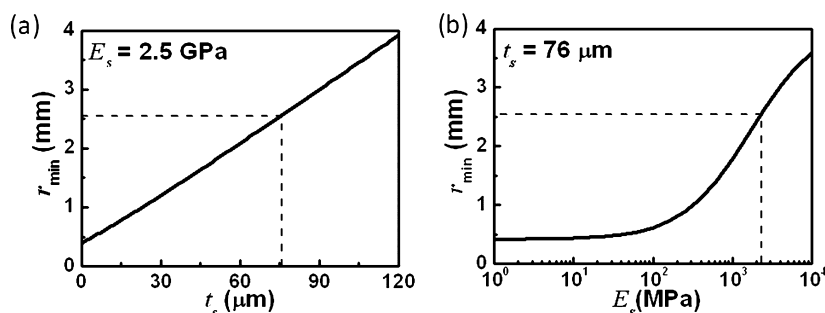
Figure 5. (a) The predicted minimum bending radius (r_{min}) as a function of the substrate thickness with substrate modulus fixed at E_s = 2.5 GPa (Kapton). (b) The predicted minimum bending radius as a function of the substrate modulus with substrate thickness fixed at t_s = 76 μm. Curves in (a) and (b) are representative of both HfO$_2$ and Al$_2$O$_3$ films. Decreasing the substrate thickness or modulus can enhance the bendability of the flexible device. The dashed lines in the figures represent the conditions closest to the current experimental samples.

substrate thickness t_s for a given substrate material, Kapton (E_s = 2.5 GPa). Since there is little effect from dielectric modulus and thickness, this curve is representative of both Al$_2$O$_3$ and HfO$_2$ thin films used in this paper under steady-state or long-term tensile strain. The plot reveals that decreasing the substrate thickness is an effective way to enhance the bendability of the flexible transistor. This is because decreased substrate thickness will shift the neutral axis closer to the dielectric layer. The linearity of the curve in Figure 5a arises from the coincidence that we are using Kapton as the substrate which has the same modulus as the liquid polyimide. If we fix the thickness of the substrate to be 76 μm and vary the substrate modulus, the minimum bending radius is shown in Figure 5b. It is clear that the softer substrate will offer better bendability. It is because decreased substrate modulus will also shift the neutral axis closer to the dielectric layer. As a result, the limiting bending radius of our sample could be as small as 0.45 mm if ultrathin or ultrasoft substrates are employed. Dashed lines in both figures highlight the conditions closest to the current experimental samples. The model predicts a minimum allowable bending radius of 2.55 mm, which is consistent with the experimental observation that gradual electrical

breakdown or complete device failure are observed at a bending radius of 2 mm for both HfO$_2$ and Al$_2$O$_3$ dielectrics respectively (Figure 3).

CONCLUSIONS

In summary, we report the first comprehensive studies of MoS$_2$ FETs using conventional solid-state high-k dielectrics on flexible substrates. Our studies yield the highest MoS$_2$ device properties on flexible substrates to date, with ON/OFF ratio greater than 10^7, subthreshold slope of ~82 mV/decade, and low-field mobility of 30 cm^2/(V·s). Furthermore, experimental investigation of the mechanical flexibility reveals that device characteristics are functional down to a bending radius of 1 mm for HfO$_2$ gate dielectric. Comparative studies of the two high-k dielectrics (Al$_2$O$_3$ and HfO$_2$) used in this research determine that HfO$_2$ affords a slower crack propagation which, in addition to its higher permittivity, makes it a more attractive gate dielectric especially for momentary device deformation. These results indicate that MoS$_2$ is likely the most suitable semiconducting material for low-power, high speed devices for flexible electronics, and smart systems owing to its unique combination of large bandgap, high mobility, and high strength.

MATERIALS AND METHODS

Material and Device Preparation. We used commercially available polyimide (Kapton) with a thickness of 76 μm as the flexible substrate, and spin-coated an additional liquid polyimide film (PI-2574 from HD Micro Systems) on the surface with a thickness of 26 μm to reduce the surface roughness. The liquid polyimide was cured at 300 °C for 1 h. Ti/Pd (2/50 nm) deposited by electron beam evaporation was used as the bottom gate electrode, and Al$_2$O$_3$ or HfO$_2$ (25 nm) deposited at 200 °C by atomic layer deposition (ALD) method as the gate dielectric. MoS$_2$ devices were prepared by mechanical exfoliation from commercial crystals (SPI supplies) onto the flexible substrate for this study. Source/drain contacts were defined by electron beam lithography, and Ti/Au (2/50 nm) were deposited by electron beam evaporation followed by the lift off process.

Material Characterization. Renishaw In-Via Raman Microscope with He−Cd blue laser (442 nm wavelength) was employed for

the Raman spectroscopy of MoS$_2$ samples. A Veeco tapping-mode atomic force microscope was used for thickness, morphology and surface analysis.

Supporting Information Available: Additional data and analysis, including device characteristics and the hysteresis of the MoS$_2$ devices, the method of extracting low-field electron mobility, Raman spectra before and after the bending test, and the

tensile strain modeling. Two videos about the propagation of cracks in both Al_2O_3 and HfO_2 are also provided. This material is available free of charge *via* the Internet at http://pubs.acs.org.

REFERENCES AND NOTES

1. Nathan, A.; Ahnood, A.; Cole, M. T.; Sungsik, L.; Suzuki, Y.; Hiralal, P.; Bonaccorso, F.; Hasan, T.; Garcia-Gancedo, L.; Dyadyusha, A.; *et al.* Flexible Electronics: The Next Ubiquitous Platform. *Proc. IEEE* **2012**, *100*, 1486–1517.
2. Reuss, R. H.; Chalamala, B. R.; Moussessian, A.; Kane, M. G.; Kumar, A.; Zhang, D. C.; Rogers, J. A.; Hatalis, M.; Temple, D.; Moddel, G.; *et al.* Macroelectronics: Perspectives on Technology and Applications. *Proc. IEEE* **2005**, *93*, 1239–1256.
3. Lee, J.; Tao, L.; Parrish, K. N.; Hao, Y.; Ruoff, R. S.; Akinwande, D. Multi-Finger Flexible Graphene Field Effect Transistors with High Bendability. *Appl. Phys. Lett.* **2012**, *101*, 252109–252109–4.
4. Chason, M.; Brazis, P. W.; Zhang, J.; Kalyanasundaram, K.; Gamota, D. R. Printed Organic Semiconducting Devices. *Proc. IEEE* **2005**, *93*, 1348–1356.
5. Geim, A. K.; Novoselov, K. S. The Rise of Graphene. *Nat. Mater.* **2007**, *6*, 183–191.
6. Petrone, N.; Dean, C. R.; Meric, I.; van der Zande, A. M.; Huang, P. Y.; Wang, L.; Muller, D.; Shepard, K. L.; Hone, J. Chemical Vapor Deposition-Derived Graphene with Electrical Performance of Exfoliated Graphene. *Nano Lett.* **2012**, *12*, 2751–2756.
7. Petrone, N.; Meric, I.; Hone, J.; Shepard, K. L. Graphene Field-Effect Transistors with Gigahertz-Frequency Power Gain on Flexible Substrates. *Nano Lett.* **2012**, *13*, 121–125.
8. Lin, Y. M.; Dimitrakopoulos, C.; Jenkins, K. A.; Farmer, D. B.; Chiu, H. Y.; Grill, A.; Avouris, P. 100-GHz Transistors from Wafer-Scale Epitaxial Graphene. *Science* **2010**, *327*, 662.
9. Ramón, M. E.; Parrish, K. N.; Chowdhury, S. F.; Magnuson, C. W.; Movva, H. C. P.; Ruoff, R. S.; Banerjee, S. K.; Akinwande, D. Three-Gigahertz Graphene Frequency Doubler on Quartz Operating Beyond the Transit Frequency. *IEEE Trans. Nanotechnol.* **2012**, *11*, 877–883.
10. Lee, J.; Parrish, K. N.; Chowdhury, S. F.; Ha, T.-J.; Hao, Y.; Tao, L.; Dodabalapur, A.; Ruoff, R. S.; Akinwande, D. State-of-the-art Graphene Transistors on Hexagonal Boron Nitride, High-k, and Polymeric Films for GHz Flexible Analog Nanoelectronics. In *IEDM Technical Digest*; IEEE: New York, 2012.
11. Schwierz, F. Graphene Transistors. *Nat. Nanotechnol.* **2010**, *5*, 487–496.
12. Neto, A. H. C.; Novoselov, K. New Directions in Science and Technology: Two-Dimensional Crystals. *Rep. Prog. Phys.* **2011**, *74*, 082501.
13. Xu, M.; Liang, T.; Shi, M.; Chen, H. Graphene-Like Two-Dimensional Materials. *Chem. Rev.* **2013**, *113*, 3766–3798.
14. Radisavljevic, B.; Radenovic, A.; Brivio, J.; Giacometti, V.; Kis, A. Single-Layer MoS2 Transistors. *Nat. Nanotechnol.* **2011**, *6*, 147–150.
15. Kim, S.; Konar, A.; Hwang, W.-S.; Lee, J. H.; Lee, J.; Yang, J.; Jung, C.; Kim, H.; Yoo, J.-B.; Choi, J.-Y.; *et al.* High-Mobility and Low-Power Thin-Film Transistors Based on Multilayer MoS_2 Crystals. *Nat. Commun.* **2012**, *3*, 1011.
16. Pu, J.; Yomogida, Y.; Liu, K. K.; Li, L. J.; Iwasa, Y.; Takenobu, T. Highly Flexible MoS_2 Thin-Film Transistors with Ion Gel Dielectrics. *Nano Lett.* **2012**, *12*, 4013–4017.
17. Das, S.; Chen, H. Y.; Penumatcha, A. V.; Appenzeller, J. High Performance Multilayer MoS_2 Transistors with Scandium Contacts. *Nano Lett.* **2013**, *13*, 100–105.
18. Yoon, J.; Park, W.; Bae, G. Y.; Kim, Y.; Jang, H. S.; Hyun, Y.; Lim, S. K.; Kahng, Y. H.; Hong, W. K.; Lee, B. H.; *et al.* Highly Flexible and Transparent Multilayer MoS_2 Transistors with Graphene Electrodes. *Small* **2013**, 10.1002/smll.201300134.
19. Bertolazzi, S.; Brivio, J.; Kis, A. Stretching and Breaking of Ultrathin MoS_2. *ACS Nano* **2011**, *5*, 9703–9709.
20. Cho, J. H.; Lee, J.; He, Y.; Kim, B. S.; Lodge, T. P.; Frisbie, C. D. High-Capacitance Ion Gel Gate Dielectrics with Faster Polarization Response Times for Organic Thin Film Transistors. *Adv. Mater.* **2008**, *20*, 686–690.
21. Lee, J.; Kaake, L. G.; Cho, J. H.; Zhu, X. Y.; Lodge, T. P.; Frisbie, C. D. Ion Gel-Gated Polymer Thin-Film Transistors: Operating Mechanism and Characterization of Gate Dielectric Capacitance, Switching Speed, and Stability. *J. Phys. Chem. C* **2009**, *113*, 8972–8981.
22. Ilic, B.; Krylov, S.; Craighead, H. Young's Modulus and Density Measurements of Thin Atomic Layer Deposited Films Using Resonant Nanomechanics. *J. App. Phys.* **2010**, *108*, No. 044317.
23. He, J.; Xu, G.; Suo, Z. Experimental Determination of Crack Driving Forces in Integrated Structures. *AIP Conf. Proc.* **2004**, 3.
24. Tsui, T. Y.; McKerrow, A. J.; Vlassak, J. J. Constraint Effects on Thin Film Channel Cracking Behavior. *J. Mater. Res.* **2005**, *20*, 2266–2273.
25. Liu, K. K.; Zhang, W.; Lee, Y. H.; Lin, Y. C.; Chang, M. T.; Su, C. Y.; Chang, C. S.; Li, H.; Shi, Y.; Zhang, H.; *et al.* Growth of Large-Area and Highly Crystalline MoS_2 Thin Layers on Insulating Substrates. *Nano Lett.* **2012**, *12*, 1538–1544.
26. Lee, Y. H.; Zhang, X. Q.; Zhang, W.; Chang, M. T.; Lin, C. T.; Chang, K. D.; Yu, Y. C.; Wang, J. T.; Chang, C. S.; Li, L. J.; *et al.* Synthesis of Large-Area MoS_2 Atomic Layers with Chemical Vapor Deposition. *Adv. Mater.* **2012**, *24*, 2320–2325.
27. Zhan, Y.; Liu, Z.; Najmaei, S.; Ajayan, P. M.; Lou, J. Large-Area Vapor-Phase Growth and Characterization of MoS2 Atomic Layers on a SiO$_2$ Substrate. *Small* **2012**, *8*, 966–971.
28. Lee, C.; Yan, H.; Brus, L. E.; Heinz, T. F.; Hone, J.; Ryu, S. Anomalous Lattice Vibrations of Single-and Few-Layer MoS_2. *ACS Nano* **2010**, *4*, 2695–2700.
29. Ghibaudo, G. New Method for the Extraction of MOSFET Parameters. *Electron. Lett.* **1988**, *24*, 543–545.
30. Fleury, D.; Cros, A.; Brut, H.; Ghibaudo, G. In *New Y-Function-Based Methodology for Accurate Extraction of Electrical Parameters on Nano-Scaled MOSFETs*, IEEE International Conference on Microelectronic Test Structures, ICMTS 2008; March 24–27, 2008; IEEE: New York, **2008**; pp 160–165.
31. Wang, H.; Yu, L.; Lee, Y.-H.; Shi, Y.; Hsu, A.; Chin, M. L.; Li, L.-J.; Dubey, M.; Kong, J.; Palacios, T. Integrated Circuits Based on Bilayer MoS_2 Transistors. *Nano Lett.* **2012**, *12*, 4674–4680.
32. Jena, D.; Konar, A. Enhancement of Carrier Mobility in Semiconductor Nanostructures by Dielectric Engineering. *Phys. Rev. Lett.* **2007**, *98*, 136805.
33. Liu, H.; Ye, P. D. MoS_2 Dual-Gate MOSFET With Atomic-Layer-Deposited as Top-Gate Dielectric. *IEEE Electron Device Lett.* **2012**, *33*, 546–548.
34. Jen, S. H.; Bertrand, J. A.; George, S. M. Critical Tensile and Compressive Strains for Cracking of Al_2O_3 Films Grown by Atomic Layer Deposition. *J. App. Phys.* **2011**, *109*, No. 084305.
35. Leterrier, Y.; Wyser, Y.; Månson, J.; Hilborn, J. A Method to Measure the Adhesion of Thin Glass Coatings on Polymer Films. *J. Adhes.* **1994**, *44*, 213–227.
36. Hsueh, C. Thermal Stresses in Elastic Multilayer Systems. *Thin Solid Films* **2002**, *418*, 182–188.

Supporting Information

High-Performance, Highly Bendable MoS$_2$ Transistors with High-K Dielectrics for Flexible Low-Power Systems

Hsiao-Yu Chang,[†] Shixuan Yang,[‡] Jongho Lee,[†] Li Tao,[†] Wan-Sik Hwang,[§] Debdeep Jena,[§] Nanshu Lu,[‡] and Deji Akinwande,[†]*

[†]Microelectronics Research Center and the Department of Electrical and Computer Engineering, The University of Texas at Austin, Austin, Texas, 78758, United States

[‡]Department of Aerospace Engineering and Engineering Mechanics, The University of Texas at Austin, Austin, Texas, 78712, United States

[§]Department of Electrical Engineering, University of Notre Dame, Notre Dame, Indiana, 46556, United States

[*]Corresponding author E-mail: deji@ece.utexas.edu

Hysteresis of MoS$_2$ devices

The hysteresis of a representative MoS$_2$ device is around 520 mV and 350 mV for V$_D$=0.1 V and 1 V respectively. The hysteresis is attributed to the unpassivated surface of devices which are measured in ambient atmosphere.
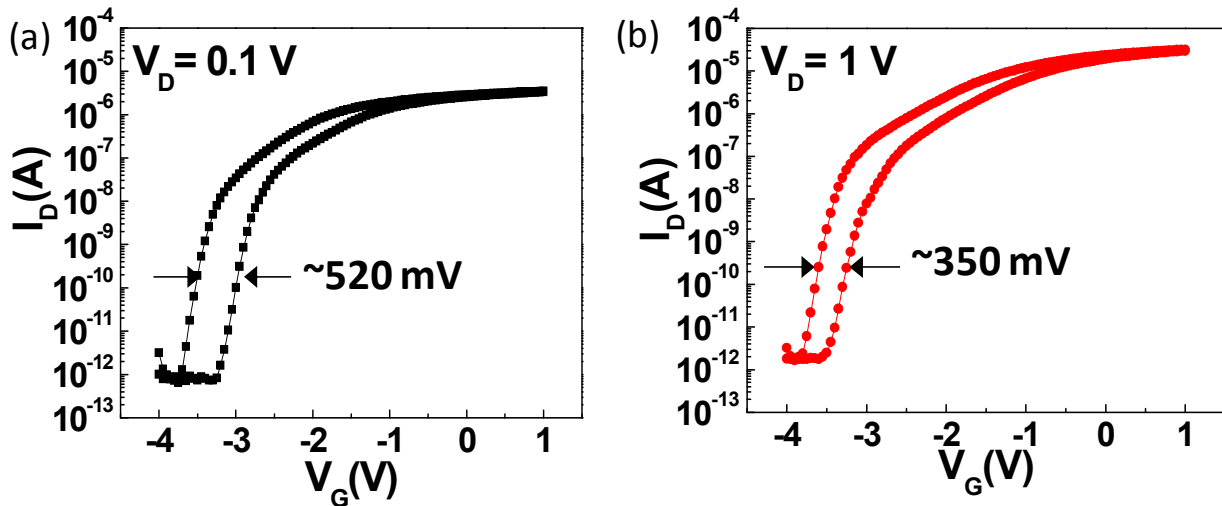

Figure S1. Hysteresis of a representative MoS$_2$ device. This is the same device reported in Figure 2 of the main text. (a) Vd=0.1V, (b) Vd=1V.

Low-field electron mobility extraction

The low-field electron mobility was extracted from the transfer characteristics using the Y-function method.[1, 2] This method has the advantage of identifying the low-field mobility without the effects of mobility attenuation phenomena that includes the impact of contact resistance (R_c). The method is based on the straightforward analysis of the drain current (I_D) in the linear region.

$$I_D = \left(\frac{\mu_o}{1 + \theta(V_G - V_T)} \right) C_{ox} \frac{W}{L} (V_G - V_T) V_D \tag{1}$$

where μ_o is the low-field mobility, θ is the effective mobility attenuation factor, C_{ox} is the gate capacitance, and W and L are the device width and length respectively. V_T is the threshold voltage, and V_G and V_D are the gate and drain voltage respectively. The transconductance (g_m) can be derived as follows,

$$g_m = \frac{dI_D}{dV_G} = \frac{\mu_o}{\left(1 + \theta(V_G - V_T)\right)^2} C_{ox} \frac{W}{L} V_D \tag{2}$$

The Y-function is defined as,[1]

$$Y = \frac{I_D}{\sqrt{g_m}} = \sqrt{\mu_o C_{ox} \frac{W}{L} V_D} (V_G - V_T) \tag{3}$$

which is a linear relation that directly affords extraction of the low-field mobility (from the slope) and the threshold voltage (from the x-intercept), since all the other parameters in the expression are known from the device and experimental conditions. Figure S2 shows the transfer characteristics and Y-function for a flexible MoS$_2$ FET (previously described in Figure 2 of the main article). Strong agreement to a linear profile is observed. The extracted μ_o = 30 cm^2/V-s, and the threshold voltage is -1.9 V. The effective mobility attenuation factor is related to the contact resistance via the following expression.[1]

$$\theta = \theta_o + \mu_o C_{ox} \frac{W}{L} R_c \tag{4}$$

where θ_o is the intrinsic mobility attenuation factor. If the intrinsic mobility attenuation factor was

3

known experimentally, then R_c could be determined directly. In the absence of accurate estimates for θ_o, an upper bound can be placed on the contact resistance in the limit of vanishing θ_o. In this limit, we determine $R_c < 33$ Ω–cm with the actual contact resistance potentially much less than this value and comparable to recent published values for metal contacted MoS$_2$ FETs.[3, 4]
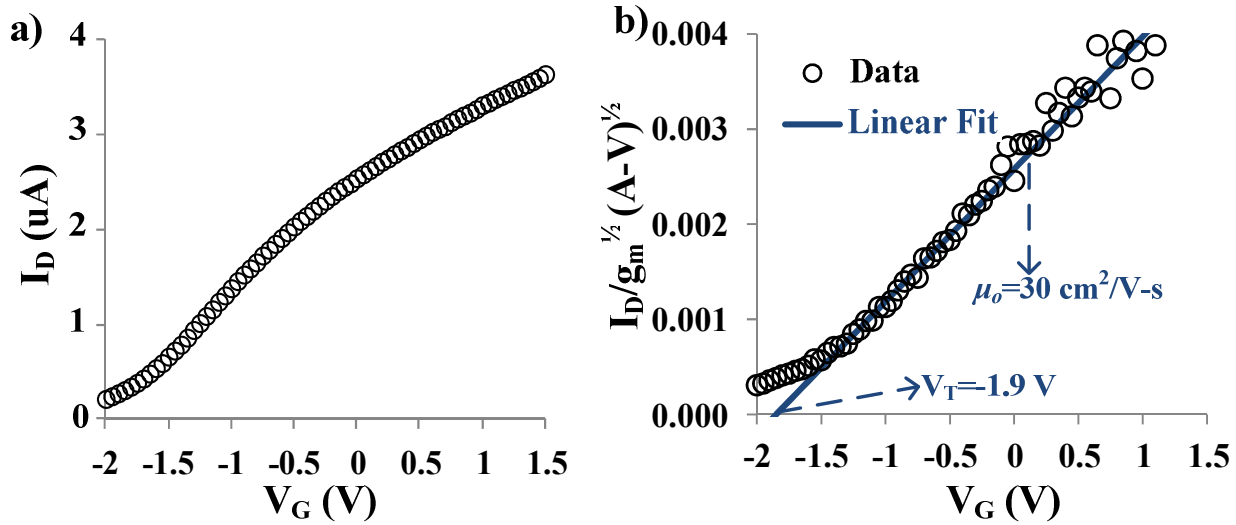

Figure S2. (a) Transfer characteristics for flexible MoS$_2$ FET made with Al$_2$O$_3$ as gate dielectric. This is the same device reported in Figure 2 of the main text. V_D=0.1 V. (b) The experimental Y-function profile showing good agreement with the expected linear profile. The extracted low-field mobility and threshold voltage are 30 cm^2/V-s and -1.9 V respectively.
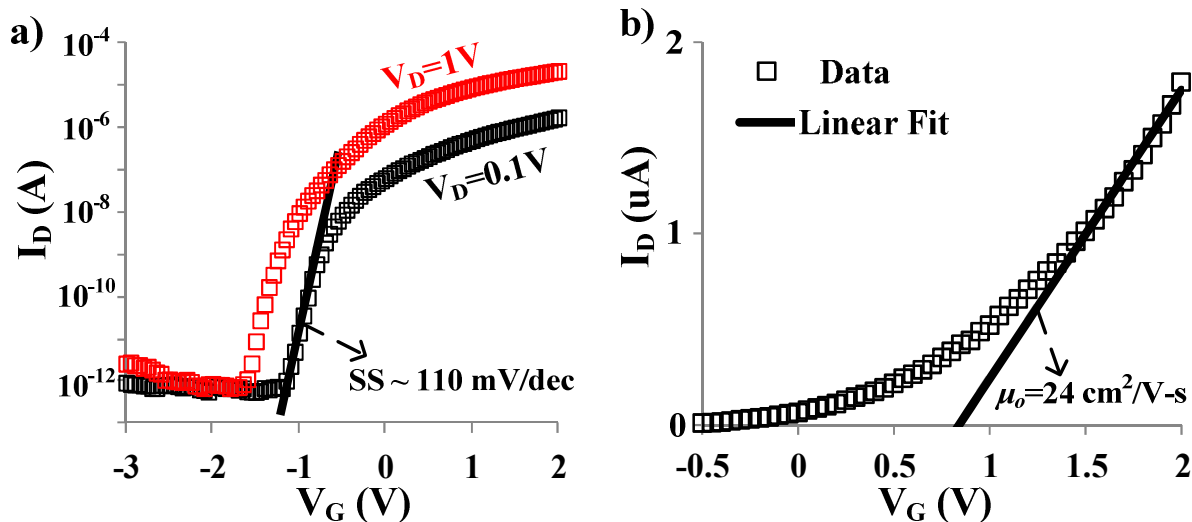
Device characteristics with HfO$_2$ as gate dielectric

Figure S3. A representative MoS$_2$ FET made with HfO$_2$ as gate dielectric on flexible PI. (a) I$_D$-V$_G$ characteristics in log scale. (b) I$_D$-V$_G$ characteristics in linear scale with an extracted low-field mobility of 24 cm^2/V-s. Device W/L = 1.25/1 μm.

The thickness dependence to the electron mobility

Based on our experimental devices within the thickness range of 7.9-21 nm, the maximum mobility occurs for a thickness of 7.9 nm, and decreases as the thickness increases. Our devices show the same trend of mobility dependence on thickness as the previous report.[5] (See Figure S4 shown below). The thickness dependence down to very thin MoS$_2$ is not known due to the poor optical contrast in identifying thin flakes. The scattered data is attributed to several effects including the variation of crystal orientation with respect to the conducting direction, the presence of defects, uncontrolled impurity contamination from the exfoliation process, the width and edge morphology of the flakes, etc. This issue requires further studies particularly on flexible substrates and will be a focus of future comprehensive research.
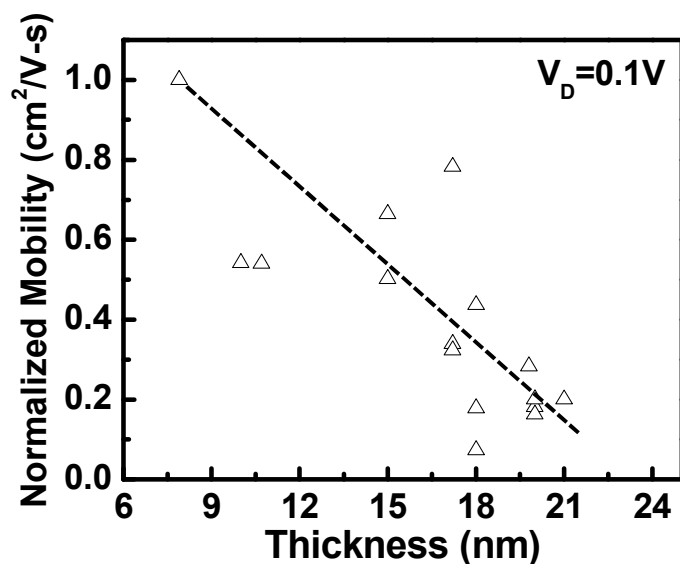
Figure S4. The thickness of MoS$_2$ versus normalized electron mobility. The mobility was normalized to the maximum mobility observed within these devices. The thickness was confirmed by AFM analysis. The dashed line is a visual guide indicating a general inverse dependence.

The intrinsic gain (g$_m$/g$_{ds}$)

The intrinsic gain (g$_m$/g$_{ds}$) is above 100 at V$_D$=0.5 V which is extracted in the current saturation region.
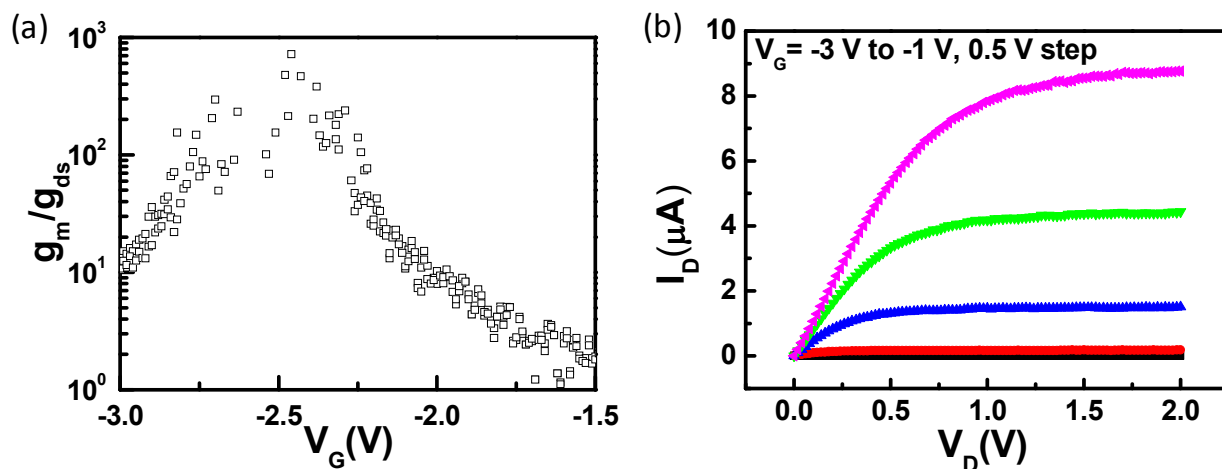
Figure S5. (a) The intrinsic gain (g_m/g_{ds}) is above 100 at V_D=0.5 V. (b) I_D-V_D characteristics show that the intrinsic gain is extracted in the current saturation region. Device W/L = 3/1 μm.

The Raman spectrum of the MoS$_2$ remains unchanged after the bending experiment
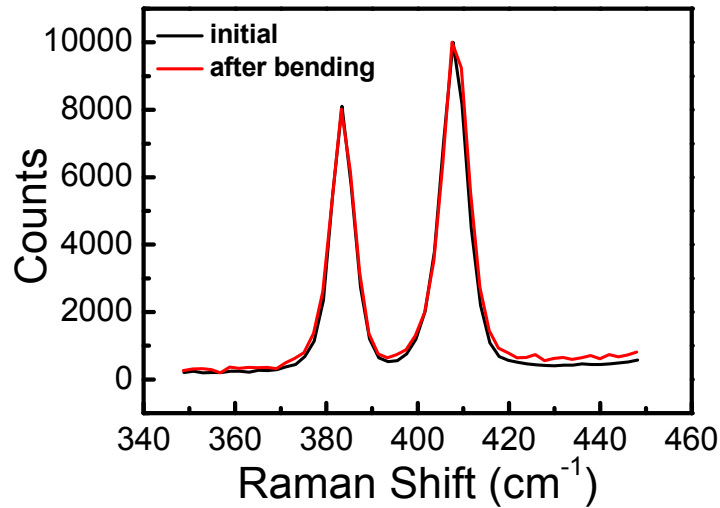

Figure S6. The Raman spectrum of the MoS$_2$ remains unchanged after the bending experiment. The minimum radius used for the bending test is 1 mm.

The AFM analysis and the optical microscope images of the MoS$_2$ FET after the bending experiment

We confirm that the MoS$_2$ remains intact by AFM after the bending test, and provide several AFM images including flakes with thickness in the range of 7.9-20.1 nm which all show the MoS$_2$ remains intact. (Figure S7 and S8) It confirms that our devices fail due to excessive leakage current from cracks in the dielectric and not by the damage to MoS$_2$. From the optical microscope images, we can also observe that clear parallel cracks are formed in the dielectric in all the devices which are responsible for

the failure of our devices. (Figure S9) One thing worth noting here is that in some occasions MoS_2 shows buckling after the bending test; however, the MoS_2 maintains good mechanical contact to the electrodes and there is no evidence of crack or damage to the structural integrity. (Figure S10)
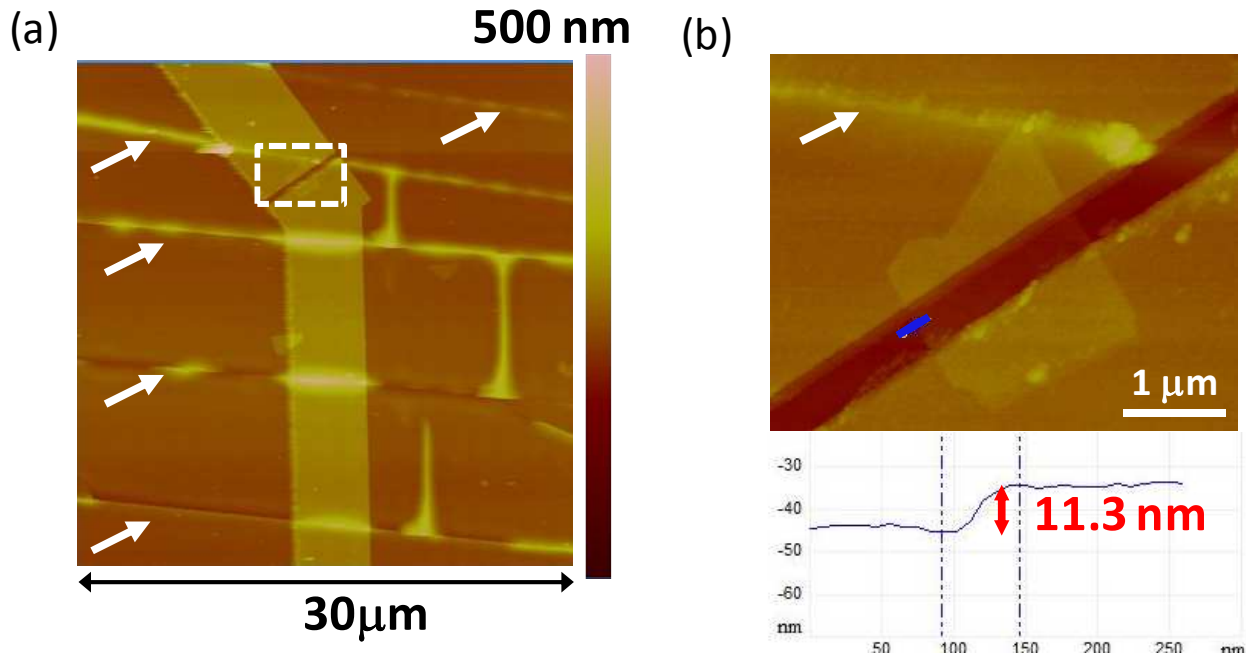

Figure S7. (a) After bending at bending radius=0.7 mm, the AFM analysis of the MoS_2 FET shows parallel cracks (marked by arrows) formed in the HfO_2. (b) The magnification of the selected device area marked in (a) shows that MoS_2 remains intact after the bending test, confirming that our devices fail by excessive leakage current but not by damage to MoS_2. The height profile is scanned along the blue line in the top picture, showing that the thickness is 11.3 nm. This AFM analysis is in agreement with the Raman spectrum in Figure S6 which indicates no observable change in the MoS_2.
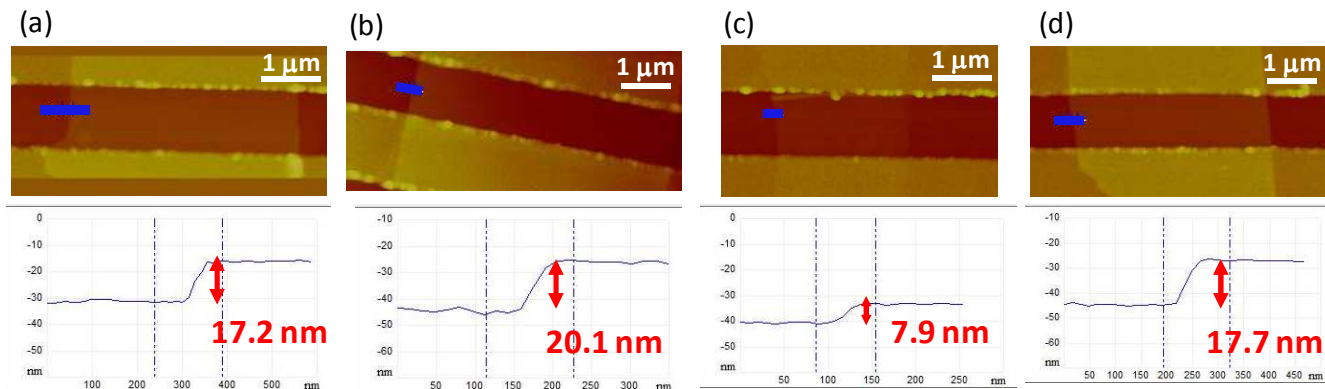
Figure S8. (a)-(d) After bending at bending radius=2 mm, MoS$_2$ with various thickness ranging from 7.9-20.1 nm remains intact. The height profiles are scanned along the blue lines marked in the top pictures. No clear correlation between the thickness of flake and the bendability is found. Devices on both HfO$_2$ and Al$_2$O$_3$ show similar results.
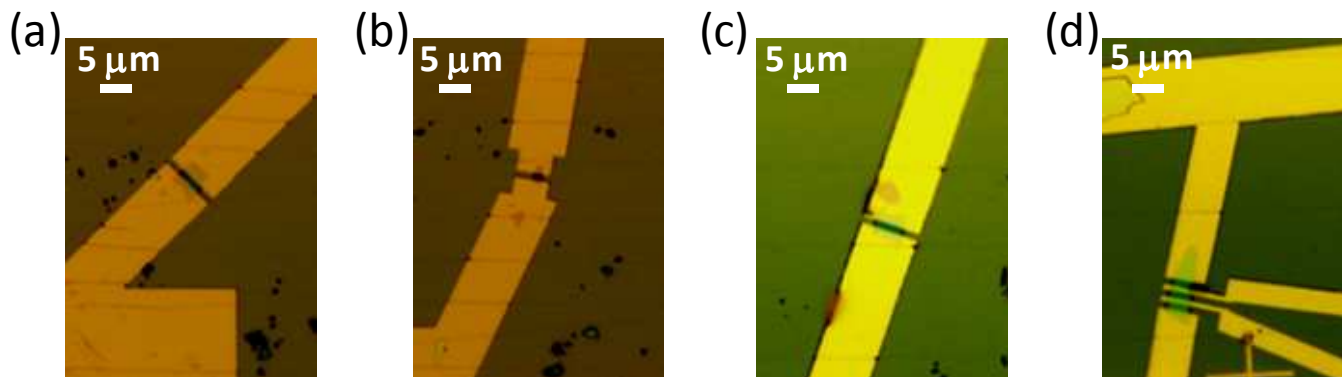

Figure S9. From optical microscope images, we can observe that clear parallel cracks are formed in the dielectric in all the devices, which is responsible for the failure of our devices. (a) (b) Devices with Al$_2$O$_3$ as the dielectric (after bending radius=1.5 mm). (c) (d) Devices with HfO$_2$ as the dielectric (after bending radius=2 mm).
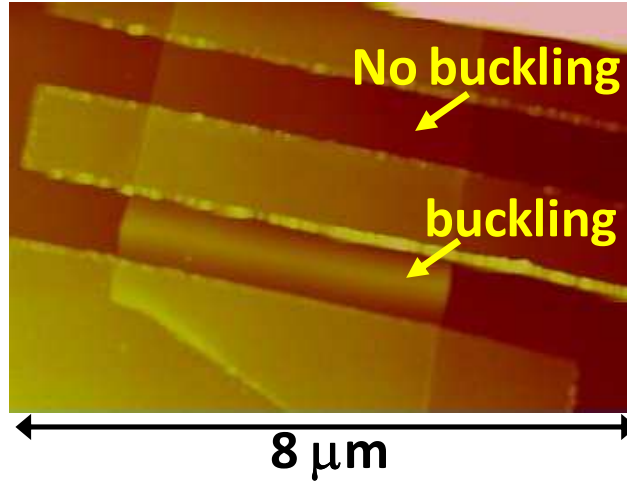
Figure S10. In some occasions, MoS$_2$ shows buckling after the bending test.

Mechanics analysis of strain induced by thermal process and bending test

The total strain in the dielectric layer (ε_{tot}) is a superposition of the thermal strain due to sample fabrication (ε_t) and the mechanical strain due to the bending test (ε_b). Here gives the detailed derivation of both strains. For the purpose of mechanical modeling, we have adopted the following material properties: $E_{Kapton} = 2.5\text{GPa}$, $\nu_{Kapton} = 0.34$, $\alpha_{Kapton} = 20\text{ppm/}^{\circ}\text{C}$,[6] $E_{PI} = 2.5\text{GPa}$, $\nu_{PI} = 0.34$,

$\alpha_{PI} = 50\text{ppm/}^{\circ}\text{C}$,[7] $E_{Pd} = 121\text{GPa}$, $\nu_{Pd} = 0.39$, $\alpha_{Pd} = 12\text{ppm/}^{\circ}\text{C}$,[8] $E_{HfO_2} = 76\text{GPa}$, $\nu_{HfO_2} = 0.2$,

$\alpha_{HfO_2} = 9.34\text{ppm/}^{\circ}\text{C}$,[9, 10] and $E_{Al_2O_3} = 167\text{GPa}$, $\nu_{Al_2O_3} = 0.21$, $\alpha_{Al_2O_3} = 8.4\text{ppm/}^{\circ}\text{C}$,[9, 11] where E is the Young's modulus, ν is the Poisson's ratio and α is the coefficients of thermal expansion (CTE).
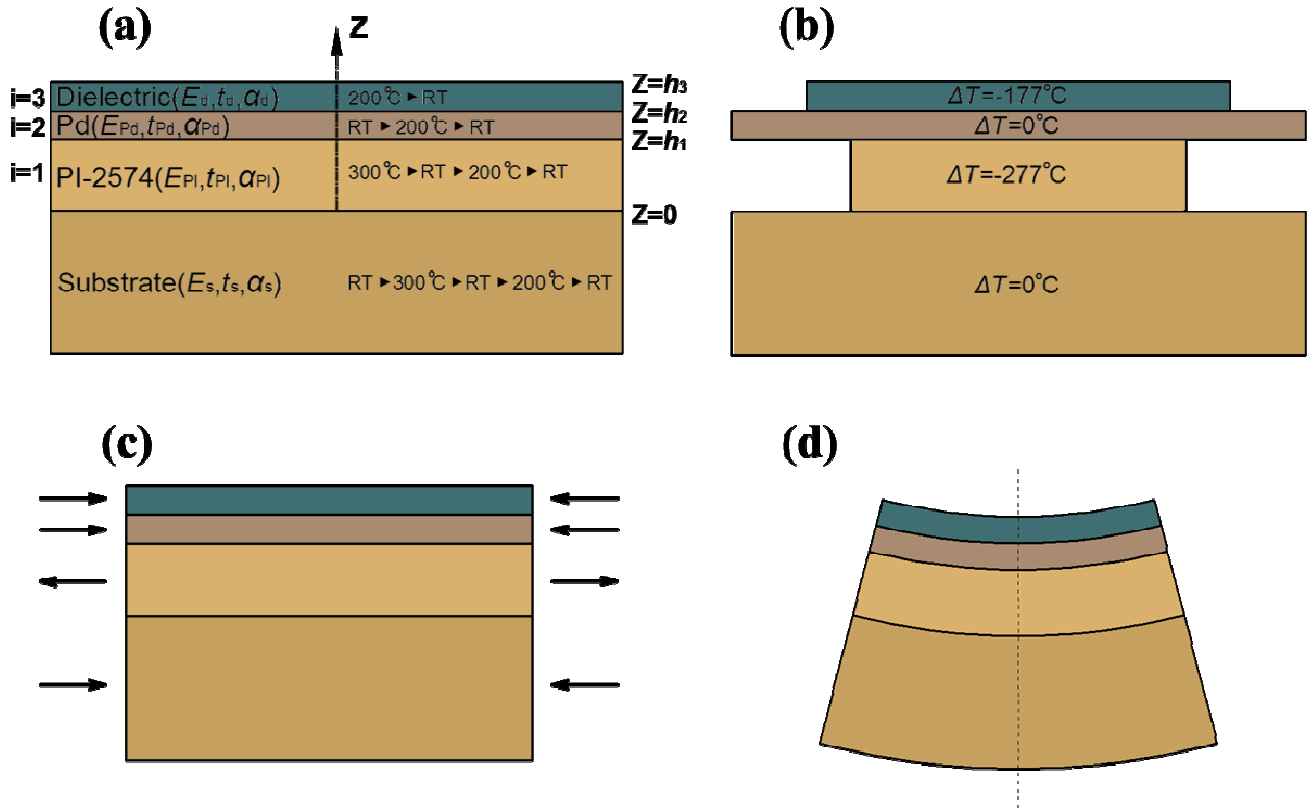
A. Thermal strain

Figure S11 Schematics to calculate thermal strain. (a) The complete multilayer stack with coordinates and the temperature history of each layer. (b) Free thermal expansion of each layer assuming no constraint between layers. (c) Stresses are applied to every layer to impose displacement compatibility. (d) The ultimate configuration of the multilayer stack due to thermal effect.

We use schematics in Figure S11 to derive thermal strains in elastic multilayer system. Assume each layer has different Young's modulus, thickness, CTE, and overall temperature change (Figure 5a). Thermal effect can be analyzed by using the overall temperature change of each layer,[12] meaning that only the difference between the initial and the final temperature of each layer is relevant.

Assume each layer of the system experiences an unconstrained differential temperature change, resulting differential elongation or shrinkage (Figure S11b). Then layer-wise uniform tension/compression is imposed on each of the layers to achieve a displacement compatibility, such that the strain in the system is a constant, c, and the net force on the system remains zero (Figure S11c).

Then bending occurs due to the asymmetric stress in the layer (Figure 5d). The total strain in the system is in the form of

$$\varepsilon = c + \frac{z - t_b}{R} \tag{S1},$$

where c is the uniform strain in each layer we imposed to achieve the displacement compatibility, R is the radius of the neutral axis, z is the distance from the top of the substrate (i.e. the bottom layer) to the position that we are interested in. The neutral axis of the whole multilayer stack is located at $z = t_b$.

Then the normal stresses in the substrate and films σ_s and σ_i are related to the total strains by

$$\sigma_s = \overline{E}_s(\varepsilon - \alpha_s \Delta T_s), \ \sigma_i = \overline{E}_i(\varepsilon - \alpha_i \Delta T_i) \tag{S2},$$

where $\overline{E}$ denotes the plane strain Young's Modulus, α is the thermal expansion coefficient and ΔT is the temperature change. The lower script s and i denote the substrate and layer i of the film, respectively.

Acknowledging the fact that, 1-the resultant force due to the uniform strain component is zero; 2-the resultant force due to the bending strain component is zero; 3-the sum of the bending moment with respect to the bending axis is zero, we are able to solve all the unknowns, which are c, t_b and r:

$$c = \frac{\overline{E}_s t_s \alpha_s \Delta T_s + \sum_{i=1}^{n} \overline{E}_i t_i \alpha_i \Delta T_i}{\overline{E}_s t_s + \sum_{i=1}^{n} \overline{E}_i t_i} \tag{S3},$$

$$t_b = \frac{-\overline{E}_s t_s^2 + \sum_{i=1}^{n} \overline{E}_i t_i (2h_{i-1} + t_i)}{2(\overline{E}_s t_s + \sum_{i=1}^{n} \overline{E}_i t_i)} \tag{S4},$$

12

$$\frac{1}{R} = \frac{3\left[\overline{E}_s(c-\alpha_s\Delta T_s)t_s^2 - \sum_{i-1}^{n}\overline{E}_i t_i(c-\alpha_i\Delta T_i)(2h_{i-1}+t_i)\right]}{\overline{E}_s t_s^2(2t_s+3t_b) + \sum_{i=1}^{n}\overline{E}_i t_i\left[6h_{i-1}^2 + 6h_{i-1}t_i + 2t_i^2 - 3t_b(2h_{i-1}+t_i)\right]} \tag{S5},$$

where t donates the thickness of the layer and h is the position of the top surface of the ith layer, i.e.

$$h_i = \sum_{k=1}^{i} t_k \ .$$

Then the strain in the dielectric layer due to the normal stress can be found as

$$\varepsilon_t = \frac{\sigma_d}{E_d} = \varepsilon_d - \alpha_d\Delta T_d = c + \frac{z_d - t_b}{R} - -\alpha_d\Delta T_d \tag{S6}.$$

It is actually the strain due to mechanical stress in as-fabricated sample but we call it ε_t because it originated from the thermal process during sample fabrication. Note in this analysis, the initial and finial status of each layer is what is relevant for analysis of the thermal effect.
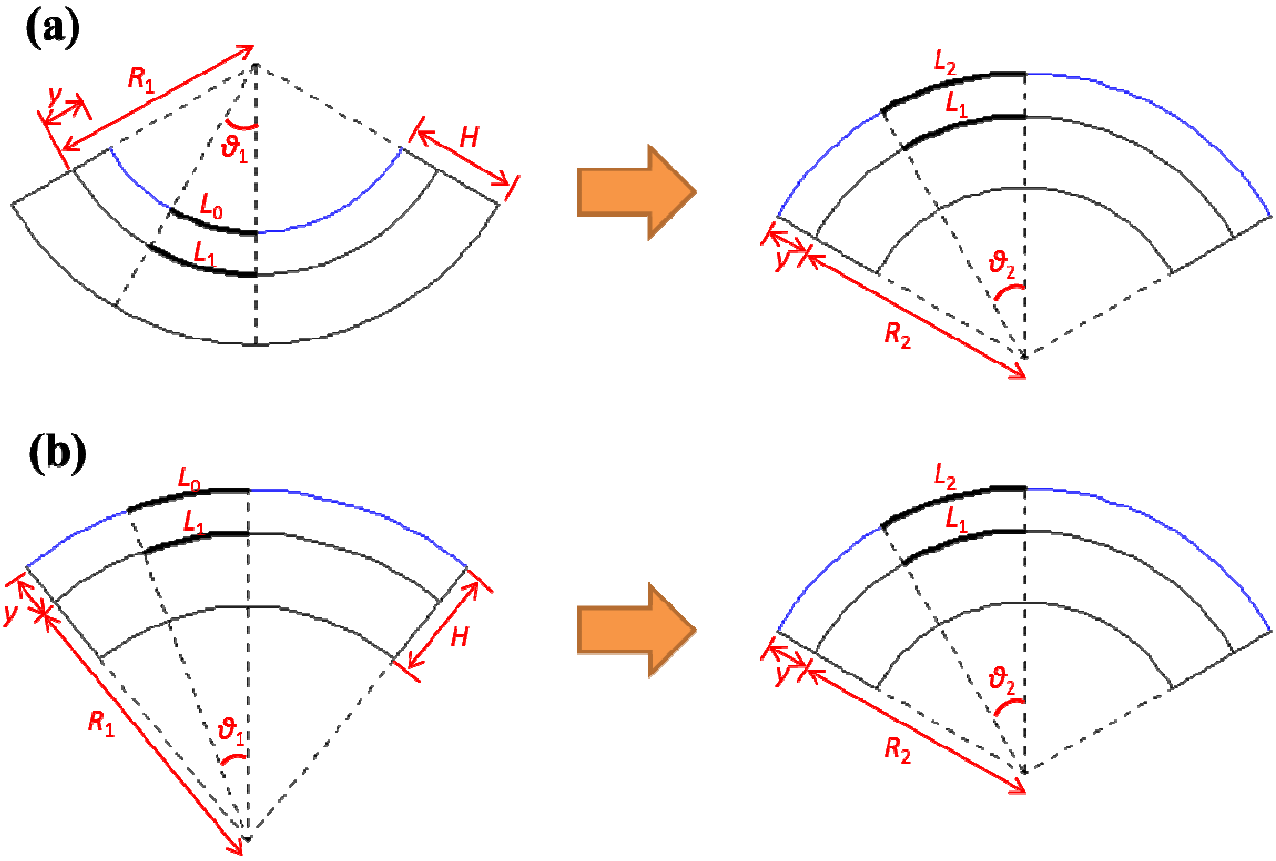
B. Bending strain

Figure S12. Schematics to help calculate the bending strain. (a) When the as-fabricated sample is bent concavely. (b) When the as-fabricated sample is bent convexly.

For trivial beam bending problem, the bending induced strain is no more than

$$\varepsilon = \frac{y}{R} \tag{S7},$$

where y is the distance from the neutral axis to the position we are interested in, and R denotes the bending radius of the neutral axis. However, Eq. S7 only holds when a beam is bent from a flat configuration to an arc. In the current problem, the as-fabricate sample is already curved (i.e. with a finite radius of curvature), we have to derive a new formula for bending strain taking this initial curvature into consideration. We assume the layers are perfectly attached to each other and all the cross-sectional planes remain planes after bending. Figure S12 shows two cases to consider. In both cases, the

bending strain by definition is given by $\varepsilon = \dfrac{L_2 - L_0}{L_0}$ where L's can be expressed by R's and θ's. Noting

the fact that neutral axis (L_1) does not change length during bending, we arrive at the following results

for Figure S12a

$$\varepsilon_b = \frac{y(R_1 + R_2)}{R_2(R_1 - y)} \tag{S8},$$

and for Figure S12b

$$\varepsilon_b = \frac{y(R_1 - R_2)}{R_2(R_1 + y)} \tag{S9}.$$
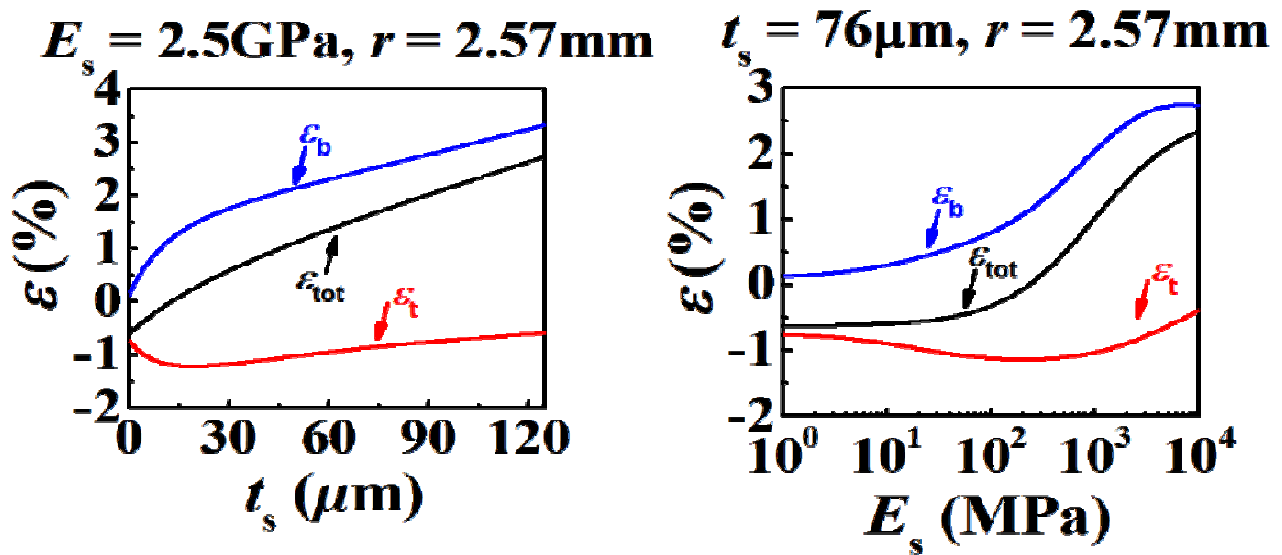
C. Total strain

Figure S13 Thermal strain, bending strain and total strain shown as functions of substrate thickness and

modulus.

Finally, the total stress-induced strain in the dielectric layer is the superposition of the thermal strain and the bending strain:

$$\varepsilon_{\text{tot}} = \varepsilon_t + \varepsilon_b \tag{S10}.$$

At a fixed bending radius of $r = 2.57$ mm ("r" measured from the bottom of the substrate to the origin, "R" measures from the neutral axis), the thermal strain, bending strain, and total strain are plotted as functions of substrate thickness (t_s) and substrate modulus (E_s) as shown in Figure S13a and S13b, respectively. Several quick conclusions can be derived from the two plots. First, bending strain increases monotonically with t_s and E_s because larger t_s or E_s is going to induce bigger y and hence bigger ε_b according to Eqs. S8 and S9. Second, due to the large CTE of the PI-2574 layer, the thermal strain/stress in the dielectric layer is always negative, but not monotonic with either t_s or E_s. Third, at given bending radius as small as $r = 2.57$ mm, although the ε_{tot} curve follows the shape of the ε_b curve pretty closely, the contribution from the thermal strain is non-trivial, and therefore cannot be neglected. Fourth, the shape of the total strain curve is monotonic, suggesting that the total strain can be reduced by reducing t_s or E_s.

The total strain is compared to the critical crack onset strain measured in Figure 4 to determine the minimum bending radius. Solving the following failure criterion equation

$$\varepsilon_t + \varepsilon_b = \varepsilon_{\text{cr}} \tag{S11}$$

will determine the minimum allowable bending radius, i.e. the bendability of the flexible transistor system. The results are plotted in Figure 5, suggesting that reducing the substrate thickness or modulus will enhance the bendability of the device. For a fixed substrate material, say Kapton ($E_s = 2.5$ GPa), Figure 5a depicts an almost linear relationship between r_{min} and t_s. This linearity is a result of numerical coincidence. As we change E_s, the shape of the curve will get distorted. Our model also predicts that when there is no substrate, i.e. $t_s = 0$ or $E_s = 0$, the minimum possible bending radius is going to

16

approach 0.45 mm. In this case, all the functional layers are simply supported by a thin layer of PI-2574 as illustrated in Figure 1c.

REFERENCES

S1.   Ghibaudo, G., New Method for the Extraction of MOSFET Parameters. *Electron. Lett.* 1988, 24, 543-545.

S2.   Fleury, D.; Cros, A.; Brut, H.; Ghibaudo, G. In *New Y-Function-Based Methodology for Accurate Extraction of Electrical Parameters on Nano-Scaled MOSFETs*, Microelectronic Test Structures, 2008. ICMTS 2008. IEEE International Conference on, 24-27 March 2008; 2008; pp 160-165.

S3.   Kim, S.; Konar, A.; Hwang, W.-S.; Lee, J. H.; Lee, J.; Yang, J.; Jung, C.; Kim, H.; Yoo, J.-B.; Choi, J.-Y.; *et al.*, High-Mobility and Low-Power Thin-Film Transistors Based on Multilayer MoS2 Crystals. *Nat. Commun.* 2012, 3, 1011.

S4.   Liu, H.; Neal, A. T.; Ye, P. D., Channel Length Scaling of MoS2 MOSFETs. *ACS nano* 2012.

S5.   Das, S.; Chen, H. Y.; Penumatcha, A. V.; Appenzeller, J., High Performance Multilayer MoS2 Transistors with Scandium Contacts. *Nano Lett.* 2013, 13, 100-105.

S6.   Kapton Datasheet.

S7.   HD Micro Systems Product Selection Guide.

S8.   Palladium: Physical Properties. http://www.webelements.com/palladium/physics.html.

S9.   Ilic, B.; Krylov, S.; Craighead, H., Young's Modulus and Density Measurements of Thin Atomic Layer Deposited Films Using Resonant Nanomechanics. *J. App. Phys.* 2010, 108, 044317-044317-11.

S10.   Samares, K.; De Gendt, S.; Houssa, M.; Landheer, D.; Misra, D.; Iwai, H. In *Physics and Technology of High-k Gate Dielectrics 5*, The Electrochemical, Society, 2007; p 569.

S11.   Aluminum Oxide, Al2O3 Material Characteristics. http://accuratus.com/alumox.html.

S12.   Hsueh, C., Thermal Stresses in Elastic Multilayer Systems. *Thin Solid Films* 2002, 418, 182-188.